International Journal of Heat and Mass Transfer 52 (2009) 2632–2645

Contents lists available at ScienceDirect

International Journal of Heat and Mass Transfer

journal homepage: www.elsevier.com/locate/ijhmt

Analysis of electrical and thermal responses of *n*-doped silicon to an impinging electron beam and joule heating

Basil T. Wong [a,1], M. Pinar Mengüç [b,*]

[a] Department of Mechanical Engineering, University of Kentucky, 318 RGAN Building, Lexington, Kentucky 40506-0108, USA
[b] Department of Mechanical Engineering, 269 RGAN Building, Lexington, KY 40506, USA

ARTICLE INFO

Article history:
Received 23 July 2008
Received in revised form 10 January 2009
Available online 23 February 2009

ABSTRACT

A detailed numerical simulation for electron-beam heating of *n*-doped silicon is presented. Electron-beam penetration is modeled using electron-beam transport equation (EBTE). The EBTE is solved by using a Monte Carlo (MC) method to determine the electron deposition distributions, including electron density deposition and optical phonon generation. Electron and phonon temperatures of the film are then determined using electron–phonon hydrodynamic equations (EPHDEs) coupled with the deposition distributions obtained from the MC simulation. The combined EBTE and EPHDEs results indicate that an electron beam creates a depletion region near the surface of incidence and causes non-equilibrium between electron and phonon temperatures.

© 2009 Elsevier Ltd. All rights reserved.

1. Introduction

Electron beams have been used extensively for material processing since 1950s [1]. A typical electron-beam energy for this application is in the order of kilo-electronvolts (keV) or mega-electronvolts (MeV) where melting and evaporation of a target material can be achieved, and hence material removal is possible. Electron beams are also used for imaging purposes and material diagnostics; in these cases, kilo-electronvolt (keV) electron beams are employed with minute amount of electric current density [2]. Effectively, the measurement and characterization of scattered electrons from the workpiece constitute the operation principles of scanning electron microscopy (SEM), transmission electron microscopy (TEM), and electron energy loss spectroscopy (EELS) applications. The ever-advancing technology in these areas has so far improved significantly understanding and modeling of electron interactions with solids, which is typically handled using the Monte Carlo (MC) simulation [3–5]. However, predicting electron and lattice temperatures of the target material as a result of electron-beam heating still requires additional research. Most of the current attempts to determine the temperature distribution of the workpiece/substrate rely on the Fourier law which assumes a linear relationship between the heat flux and the temperature gradient. Using this classical, yet simple approach, the coupling between the electron beam and heat conduction is achieved, where electrons and the lattice are assumed to be at the same temperature [6,7]. In more recent studies, the so-called two-temperature model is employed where separate electron and phonon temperatures are considered [8]. These approaches are applicable if the electron removal from the material due to the generation of secondary electron is not significant and when there are no applied voltages across the material. If the electron removal is significant that causes changes to the local electron density, both the electron and phonon temperature distributions would be altered, and neither the classical Fourier Law nor a two-temperature model would be able to simulate the physics. In this paper, we aim to consider such a complex case where the electrons received from an electron beam and the electrons due to the applied voltage are considered to alter the energy balance in *n*-doped silicon.

In previous studies, we have already coupled the electron-beam transport equation (EBTE), solved using the MC simulation [4,5,9,10] with the classical and two-temperature heat conduction equations to study the heating effect of energetic electron beams [6–8]. These simulations have shown that local temperatures of the target material (or workpiece) could be elevated significantly when an electron beam with high energy flux was utilized. However, in these studies, and the density of the external electrons (i.e., from the electron beam) were not included, implying that charge accumulation (or depletion) was neglected. In order to determine these additional effects induced by an electron beam, a modified electron-beam MC simulation, which can predict the deposition of electron population and energy on a target material, is required. These deposition distributions describe the physics of high-energy electron propagation. When electrons are attenuated to lower energy levels, the effects of thermal conduction and electric field become dominant in the transport. This is where the electron–phonon hydrodynamic equations (EPHDEs) [5,11] take over

* Corresponding author. Tel.: +1 (859) 257 6336x80658; fax: +1 (859) 257 3304.
E-mail addresses: btung01@engr.uky.edu (B.T. Wong), menguc@engr.uky.edu (M.P. Mengüç).
[1] Tel.: +1 (859) 257 6337x80697.

0017-9310/$ - see front matter © 2009 Elsevier Ltd. All rights reserved.
doi:10.1016/j.ijheatmasstransfer.2009.01.007

Nomenclature

a_0	Bohr radius [m]
B	Gaussian distribution [-]
C	heat capacity [J/m^3 K]
c	speed of light [m/s]
E	electron energy [eV]
E_{beam}	initial electron-beam energy [eV]
E	electric field vector [V/m]
E	coulomb charge [C]
$\hbar$	reduced Planck's constant [J s]
k	electron wave number [1/m]
k	thermal conductivity [W/m K]
k_B	Boltzmann's constant [eV/K or J/K]
l	mean free path [m]
I	intensity [W/m^2 sr]
I_{beam}	electric current of the electron beam [C/s]
m	mass of electron [kg]
n	electron density [1/m^3]
N	total number of statistical ensembles [-]
P_e	electron momentum [kg m/s]
Q	scattering cross section [m^2]
q	wave number (loss or gain) [1/m]
R	cumulative probability distribution function [-]
Ran	a random number [-]
R_{beam}	$1/e^2$-radius of the Gaussian distribution [m]
S	scattering distance [m]
T	temperature [K]
T	transmission function [-]
U_0	surface potential ($=E_F + \Phi$) [eV]
v	velocity [m/s]
dV	volume of a computational element [m^3]
W	total average electron energy (i.e., internal + kinetic) [eV]

Symbols

β	angle with respect to surface normal [rad]
ϕ	electric potential [V]
ω	frequency [rad/s]
ε	permittivity [F/m]
τ	relaxation time [s]
Θ	scattering angle [rad]
σ	scattering coefficient [1/m]
Ω	solid angle [sr]
Φ	work function [eV]
Φ_e	electron phase function [-]

Subscripts

A	acoustic
D	doped
e	electron
eff	effective
el	elastic
F	Fermi
inel	inelastic
LO	longitudinal optical
m	momentum
MC	Monte Carlo
Nor	normalized
ph	phonon

Superscripts

′	indicates after collision/scattering
prev	previous

the role of describing the physics of low-energy electron propagation. Therefore, results from the MC simulations of the EBTE need to be coupled with EPHDEs so that heating effect of the electron beam can be studied thoroughly in terms of electric field and thermal gradient generated by the electron beam. These models are discussed thoroughly in the next section.

2. Numerical solution methodology

In this paper, we specifically consider the heating of *n*-doped silicon (as a workpiece) by a continuous electron beam with prescribed spatial beam width, energy, and electric current. The electron beam is assumed to be originated from any electron source with known initial kinetic energy, E_{beam}. The beam is directed perpendicularly on the workpiece and its area of incidence follows a Gaussian distribution with a $1/e^2$-radius (denoted as R_{beam}). The dimensions are selected such that the workpiece is considered as semi-infinite in width and depth for the electron-beam propagation, and hence electron transmission is not permitted. A simple schematic of the problem is depicted in Fig. 1.

A flowchart of the numerical solution methodology employed by this study is depicted in Fig. 2. In order to determine the temperature distribution inside the workpiece, there are two aspects of the problem to be investigated. First, the modeling of electron-beam propagation is required following the EBTE, which includes predictions of electron-density deposition and optical-phonon generation as the electron beam transfers energy and momentum to the material along the penetration path. A MC simulation of the EBTE is used for this purpose. Since the initial electron-beam energy is in the order of sub-kilo-electronvolts (keV), which are naturally much higher than the energy change induced by the temperature gradient and the electric field considered in this application, it is possible to model the electron-beam propagation independently and obtain a steady-state electron deposition distributions, which are then treated as source generations in the EPHDEs. The EPHDEs then determine the electric field, electron density and velocity, and temperature distributions of electrons and phonons (i.e., optical and acoustic) inside the material by coupling propagations of all these heat carriers accordingly. This is the approach that the current work emphasizes on. However, if the electron-beam heating is to be solved rigorously and this would be the case when the temperature gradient and the electric field become

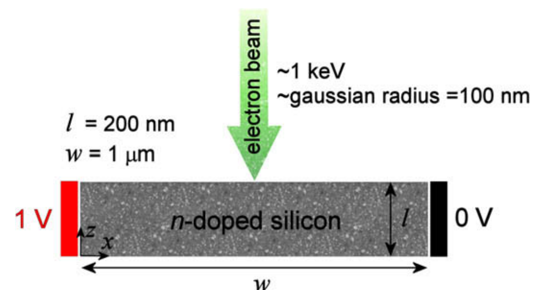

Fig. 1. A simple schematic illustrating the physical problem and several parameters considered in the simulation: an electron beam impinges perpendicularly on a gold workpiece.

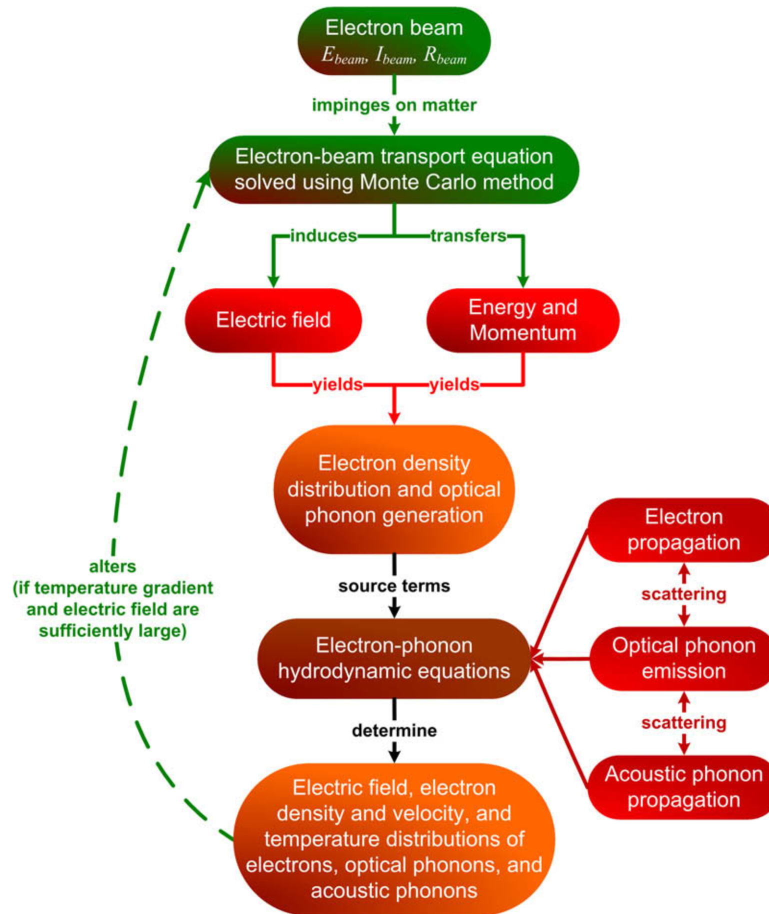

Fig. 2. The numerical solution methodology employed in the current study is given, detailing the coupling between solutions of the EBTE and EPHDEs. The scenario indicated by the dash line is not considered in this study.

large enough to affect the beam, the electron-beam propagation needs be solved simultaneously with the EPHDEs where electron and phonon temperatures affect the electron-beam deposition rate, and vice versa. This may require iterations between solutions of the MC simulation and the EPHDEs, which is beyond the scope of the current work and can be investigated in the future to enhance the present concept.

2.1. Monte Carlo simulation of electron-beam transport equation

Our first objective is to determine the electron deposition profiles, such as the electron density and optical-phonon generation within the material. In order to achieve this goal, the EBTE needs to be solved along the beam path. Without any external electric field applied to the beam, the EBTE can be expressed as [5]:

$$\frac{\partial I_e}{\partial t} + \vec{v}_e \cdot \nabla_{\vec{r}} I_e = -[\sigma_{inel}(E) + \sigma_{el}(E)]\, v_e I_e + \frac{\int_{E'} \int_{\Omega'} [\sigma_{inel}(E')\Phi_{inel}(E', \Omega' \rightarrow E, \Omega) I'_e v'_e] d\Omega' dE'}{4\pi} + \frac{\int_{E'} \int_{\Omega'} [\sigma_{el}(E')\Phi_{el}(E', \Omega' \rightarrow E, \Omega) I'_e v'_e] d\Omega' dE'}{4\pi}, \tag{1}$$

which is similar to the radiative transfer equation (RTE) except that the scattering properties are dependent on electron energy [10]. The EBTE is an integro-differential equation, and it is cumbersome to obtain an analytical (or even numerical) solution without imposing any simplification to the intensity of the beam. The best method of solving this type of equation is to use a statistical approach, which is often termed the MC method. In this study, a MC simulation algorithm for electron-beam propagation is developed using the Mott's elastic scattering cross section [12] and the Penn's dielectric function [13,14]. This MC simulation is different from our previous published work in terms of treating absorption and scattering of the electron beam, and it is an improved version. The MC simulation basically determines the trajectories of electrons originated from the electron beam as they go through a series of elastic and inelastic scattering events by atoms and electrons inside the material. Electrons are traced until their energies become low enough where electron–phonon scattering becomes dominant, and that the electrical and thermal responses of the material become important in describing the low-energy electron transport.

First, we provide a brief summary of the MC simulation procedures; details can be found elsewhere [3,5,9,10]. A MC simulation starts with initializations of statistical ensembles such as the initial electron energy, launching location, and penetrating direction. These statistical ensembles represent a tiny fraction of the entire electron beam in terms of energy. The simulation proceeds with launching of these ensembles one after another independently until the last ensemble. The wave interference effect is not accounted in the simulation since the wavelength of the electron beam considered is much smaller than the characteristic length of the target object.

A Gaussian distribution is considered for the incident electron beam, given:

$$B(r) = \frac{2}{\pi R_{beam}^2} e^{-2(r/R_{beam})^2}, \tag{2}$$

where the exponential is equal to $1/e^2$ at R_{beam}. Even though a spatial Gaussian profile is assumed for electron beam, we do not consider any temporal variation, meaning that the beam power is always continuous. In the MC simulation, r is decomposed into x and y so that the Cartesian coordinate is used to keep track of the positions of the ensembles. To obtain MC results for an electron beam following a Gaussian distribution, results are first obtained for the case where all the ensembles are launched in the exact same position (i.e., impulse beam profile). Convolution is then used between these results and the Gaussian beam profile given in Eq. (2) to generate final desired results. This method is generally more efficient since the number of ensembles required to compute smooth statistical distribution is lesser.

In MC simulations, each statistical ensemble is tracked until either it exits the medium or its energy falls below a threshold value (=$E_{threshold}$). The threshold value is chosen to be the band gap of silicon in this case, which is approximately 1 eV. After launching, statistical ensembles suffer a series of scattering events within the medium. These events can be either elastic or inelastic depending on the various scattering probabilities derived according to the properties of the material and random numbers. Elastic scattering simply redirects the propagating direction of an ensemble while inelastic changes its energy in addition to its direction.

Each statistical ensemble is allowed to travel for a certain amount of distance before it is scattered elastically or inelastically by the medium. This distance is termed the scattering distance, S_{eff}, and its cumulative probability distribution function (CPDF) is given as:

$$R(S_{eff}) = \exp(-S_{eff}/l_{eff}), \tag{3}$$

where l_{eff} is the effective mean free path computed from elastic and total inelastic mean free path (i.e., l_{el} and $l_{inel,total}$, respectively):

$$l_{eff}^{-1} = l_{el}^{-1} + l_{inel,total}^{-1}. \tag{4}$$

The total inelastic scattering mean free path includes that of the optical phonon emission, $l_{inel,LO}$, and the mean free path of electron–electron scattering, $l_{inel,e\text{-}e}$. By inverting Eq. (3) and replacing the CPDF with a random number, the scattering distance can be expressed as

$$S_{eff} = -l_{eff} \ln(Ran_S), \tag{5}$$

where Ran_S is a random number.

Upon interaction, another random number, $Ran_{l,1}$, is used to determine whether the event is elastic or inelastic. The electron is scattered elastically if $Ran_{l,1} < l_{el}^{-1}/l_{eff}^{-1}$ and inelastically if $Ran_{l,1} \geqslant l_{el}^{-1}/l_{eff}^{-1}$. If the scattering is inelastic, an additional random number, $Ran_{l,2}$, will be drawn to determine whether it is of electron–electron interaction or optical phonon emission. If $Ran_{l,2} \geqslant l_{inel,LO}^{-1}/l_{inel,total}^{-1}$, it is an electron-electron scattering; otherwise it is an optical phonon emission. When the inelastic scattering is of electron–electron type, the amount of kinetic energy loss needs to be determined from the probability of inelastic scattering per unit length and energy change (i.e. $dl_{inel}^{-1}/d(\Delta E')$). The CPDF for the amount of energy change is then expressed using this probability as [3,5]:

$$R = \int_0^{\Delta E} \frac{dl_{inel}^{-1}}{d(\Delta E')} d(\Delta E') \Big/ \int_0^{E-E_F} \frac{dl_{inel}^{-1}}{d(\Delta E')} d(\Delta E'), \tag{6}$$

The limits of the integration correspond to the possible amount of kinetic energy loss of electrons, which ranges from none to the difference between the current kinetic energy E and the Fermi energy E_F of the target material. Next the scattering direction is determined according to the type of the scattering event. The CPDF of the elastic scattering is derived from the Mott scattering cross section, while the CPDF of the inelastic scattering requires the use of dielectric theory.

The above MC simulation procedures remain unaltered for any given material except the scattering properties. These properties change depending on the material and are discussed in the next section. Several details regarding the MC simulation procedures, for example, the derivation of the direction cosines needed for tracking the ensembles and sampling techniques for the scattering direction, are not mentioned to keep the manuscript within reasonable length. These derivations are outlined by Wang et al. [15], Ding and Shimizu [3], and Wong and Mengüç [5].

2.1.1. Elastic scattering (Mott cross section)

The electron scattering properties are the most crucial information in simulating electron-beam propagation for different types of materials. Elastic and inelastic scattering properties are needed in the simulation; each requires different derivation to represent the scattering process with correct physics. Elastic scattering probability is obtained from Mott's scattering cross section while inelastic scattering probability is derived from the Penn's dielectric function. The Mott elastic differential scattering cross section without the polarization effect is typically expressed in the form [12]:

$$\frac{dQ_{el}(\Theta, k)}{d\Omega} = |f|^2 + |g|^2. \tag{7}$$

The scattering factors f and g are functions of a scattering polar angle Θ, and they are given as:

$$f(\Theta, k) = \frac{1}{2ik} \sum_{l=0}^{\infty} \left\{ (l+1)[e^{2i\delta_{-l-1}} - 1] + l\left[e^{2i\delta_l} - 1\right] \right\} P_l(\cos\Theta), \tag{8}$$

$$g(\Theta, k) = \frac{1}{2ik} \sum_{l=1}^{\infty} \left[-e^{2i\delta_{-l-1}} + e^{2i\delta_l} \right] P_l^*(\cos\Theta). \tag{9}$$

Here, P_l's and P_l^*'s are the ordinary Legendre polynomials and the associated Legendre polynomials, respectively, and δ_l's are the Dirac phase shifts. The Dirac phase shifts are obtained by solving the Dirac equation, which describes the relativistic behavior of an electron, including its spin, the magnetic moment of the electron, and the spin–orbit coupling. Details on how to derive and solve the Dirac equation are described by Lin et al. [16]. In Eqs. (9) and (10), k represents the wave number of the electron with energy E. They are related according to:

$$k^2 = \frac{(E^2 - m^2c^4)}{\hbar^2 c^2}, \tag{10}$$

where $\hbar$ is angular Planck's constant, c is the speed of light, and m is the mass of electrons. Once the elastic scattering cross section is determined from Eq. (7), the scattering phase function is calculated as [5]:

$$\Phi_{el}(\Theta, E) = \frac{4\pi}{Q_{el,total}(E)} \frac{dQ_{el}(\Theta, E)}{d\Omega}, \tag{11}$$

where

$$Q_{el,total}(E) = \int_{\Omega=4\pi} \frac{dQ_{el}(\Theta, E)}{d\Omega} d\Omega, \tag{12}$$

Since it is difficult to invert Eq. (7) directly to obtain a scattering angle Θ, a look-up table listing the CPDF and the corresponding Θ is needed. This way, whenever a random number of drawn, a corresponding Θ can be found from the table (see Wong and Mengüç [5] for details). The elastic mean free path of the electron is derived from the following expression:

$$l_{el}(E) = \frac{A}{N_a \rho Q^{el}_{e,total}(E)}, \tag{13}$$

where A is the atomic weight, N_a the Avogadro number, ρ the density of the material, and $(N_a\rho/A)$ the number of atoms per unit volume. Table of Mott scattering cross section data are made available by Joy [17]; these data are used in the current MC simulations.

2.1.2. Inelastic scattering (Penn's dielectric function)

In the event of inelastic scattering, electrons lose kinetic energy and change direction of propagation. The direction change of the electron by this type of scattering mechanism is typically small. The inelastic scattering probability can be derived from the energy-loss function at different energy levels or wavelengths. Since the energy-loss function is a measure of responses of electrons and atoms in a medium as a whole when the medium is exposed to an external disturbance, it can be considered as more accurate compared to other independent formulations. Therefore, having accurate optical constants of the material is very important since the energy-loss function is derived from the optical constants at different energy levels.

The dielectric formulation starts from the double differential inelastic scattering cross section, which is expressed as [14]:

$$\frac{d^2 l^{-1}_{inel}}{d(\hbar\omega)dq} = \frac{1}{\pi a_0 E}\mathrm{Im}\left[-\frac{1}{\varepsilon(q,\omega)}\right]\frac{1}{q}. \tag{14}$$

The imaginary part (denoted as Im[·]) of the negative inverse of the dielectric function $\varepsilon(q,\omega)$ in the equation describes the probability of energy loss. It is an extrapolated energy-loss function for different wave number, q, and frequency, ω, obtained by deriving from the energy-loss function at $q = 0$. The energy-loss function of silicon used in this work is shown in Fig. 3, which is derived from the optical data provided by Palik [18]. The probability of an electron suffering an inelastic scattering event per unit path length and per unit energy change is then obtained using Eq. (14) after integration over all possible wave numbers q of the excited plasmons, and using the energy and momentum transfer conservation, which is given as [3]:

$$\begin{aligned}\frac{dl^{-1}_{inel}}{d(\Delta E)} &= \frac{1}{\pi a_o E}\\ &\times \int_0^\infty \left\{\frac{\hbar\omega_p}{(\Delta E)^2 - (\hbar\omega_p)^2 + [(\hbar\bar{q})^2/2m_0]^2}\mathrm{Im}\left[\frac{-1}{\varepsilon(\omega_p)}\right]\right.\\ &\left.\times\Theta\left[\frac{\hbar^2}{2m_0}(2k\bar{q}-\bar{q}^2)-\Delta E\right]\right\}d(\hbar\omega_p),\end{aligned} \tag{15}$$

if the following plasmon dispersion equation is assumed [13]:

$$\omega_q^2(q,\omega_p) = \omega_p^2 + \frac{1}{3}v_F^2(\omega_p)q^2 + \left(\frac{\hbar q^2}{2m_0}\right)^2. \tag{16}$$

Here, $\bar{q}$ is the positive solution of the dispersion relation $\omega = \omega_q(\bar{q},\omega_p)$, $E = (\hbar k)/2m$ and $\Delta E = \hbar\omega$. The inelastic mean free path of the electron can then be obtained by integrating the cross section over all energy changes:

$$l^{-1}_{inel} = \int_0^{E-E_F}\frac{dl^{-1}_{inel}}{d(\Delta E)}d(\Delta E). \tag{17}$$

Note that l_{inel} depends on the kinetic energy of the electrons. Details of the derivation of the inelastic scattering cross section are readily available elsewhere [3].

2.1.3. Electron-optical-phonon scattering

Electron-optical-phonon (e-LO) scattering is important as it is this mechanism which allows the electron beam to lose its energy to the lattice. If energy from the electron beam is transferred to the lattice, the temperature of the target material is increased. This increase can be slow or abrupt depending on the spatial current density of the beam. To be able to include the electron–phonon scattering in the MC simulation, a proper derivation of scattering probability is needed. A simple expression is used for the scattering probability, and the e-LO scattering rate is derived using [19]:

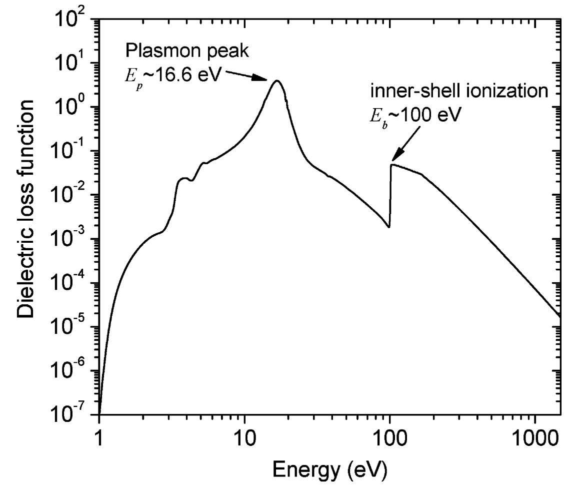

Fig. 3. The dielectric loss function as derived from the optical data found in handbook compiled by Palik [18].

$$\frac{1}{\tau_{\text{e-LO}}} = \frac{m_e^{1.5}\varphi^2}{\sqrt{2}\pi\rho\hbar^3\omega_0}\left[f\sqrt{E+\hbar\omega_0} + (f+1)\sqrt{E+\hbar\omega_0}\right], \tag{18}$$

where ϕ is the optical deformation potential, assumed to be 9 eV/Å for silicon [20]. When an electron undergoes an e-LO scattering, a LO-phonon is more likely to be created than destroyed, since electrons from the electron beam possess relatively high energy. Therefore, an electron is assumed to lose a fixed amount of energy when such scattering occurs, which corresponds to LO-phonon energy in the material (i.e., 62 meV for silicon [21,22]). Electrons also lose energy by creating secondary electrons and generating LO-phonons until their energies fall below the threshold energy. By tracking the motion of these electrons, we can determine the electron density and the LO-phonon generation inside the thin film and account for these distributions in the EPHDEs where temperature field can be computed.

2.1.4. Calculations of electron density deposition and optical phonon generations

In the MC simulation, each statistical ensemble represents a fraction of total electrons and energy originated from the electron beam. In order to compute the electron deposition distributions, these quantities are tracked continuously in the simulation. The electron density accumulated at various locations within the medium can be easily accounted for since each statistical ensemble represents a fixed number of electrons. Whenever an ensemble exits the workpiece, its energy is considered as a loss. However, when the energy of the ensemble falls below the threshold limit, the electron density at that particular location will be updated accordingly, and hence contribute to the total electron density deposition distributions:

$$n^{current}_{MC,total}(x,y,z) = n^{prev}_{MC,total}(x,y,z) + 1. \tag{19}$$

In the case of optical phonon generations by the energetic electrons, the storing array for the generation is updated at the position where an optical phonon is emitted, which is expressed as:

$$E^{current}_{MC,total}(x,y,z) = E^{prev}_{MC,total}(x,y,z) + \hbar\omega_{LO}. \tag{20}$$

Table 1
List of thermophysical properties of silicon used in the simulation.

Thermophysical properties	Equations and parameters	Reference(s)
Electron momentum relaxation time, τ_m	$\tau_m = a + b(\gamma - 1) + c\exp[-d(\gamma - 1)][\mathrm{ps}]\gamma = W_e/0.025; a = 0.0681;$ $b = -0.0023; c = 0.2051; d = 0.9547$	Romano and Russo [29]
Electron thermal conductivity, k_e	$k_e = \frac{n_e \tau_m k_B^2 T_e}{m_e}(r + 2.5)[\mathrm{W/m\ K}]; r = -2$	Majumdar [19]
Electron-optical-phonon relaxation time, $\tau_{\text{e-LO}}$	$\tau_{\text{e-LO}} = a + b(\gamma - 1) + c\exp[-d(\gamma - 1)][\mathrm{ps}]\gamma = W_e/0.025; a = 0.1731;$ $b = 0.0313; c = 0.2382; d = 0.5167$	Romano and Russo [29]
Optical-acoustic phonon relaxation time, $\tau_{\text{LO-A}}$	8 [ps]	Majumdar [19]
Optical phonon heat capacity, C_{LO} (Einstein's model)	$C_{\mathrm{LO}} = 3\eta k_B(\frac{\theta_{\mathrm{LO}}}{T_{\mathrm{LO}}})^2 \frac{\exp(\theta_{\mathrm{LO}}/T_{\mathrm{LO}})}{[\exp(\theta_{\mathrm{LO}}/T_{\mathrm{LO}})-1]^2}[\mathrm{J/m^3 - K}]\hbar\omega_{\mathrm{LO}} = 62[\mathrm{meV}];$ $\theta_{\mathrm{LO}} = \frac{\hbar\omega_{\mathrm{LO}}}{k_B} = 720[\mathrm{K}]\eta = \frac{6.02\times10^{23}[\mathrm{atoms/mol}]\times2{,}330[\mathrm{kg/m^3}]}{28\times10^{-3}[\mathrm{kg/mol}]} = 5.01\times10^{28}[\mathrm{atoms/m^3}]$	Majumdar [19], Ziman [30]
Acoustic phonon heat capacity, C_{A} (Debye's model)	$C_{\mathrm{A}} = 9\eta k_B(\frac{T_{\mathrm{A}}}{\theta_{\mathrm{D}}})^3 \int_0^{\theta_{\mathrm{D}}}/T_{\mathrm{A}} \frac{x^4 e^x}{(e^x-1)^2}dx[\mathrm{J/m^3\ K}]\theta_{\mathrm{D}} = 625[\mathrm{K}]$	Ziman [30]
Acoustic phonon thermalconductivity, k_{A}	$k_{\mathrm{A}} = \frac{1.585\times10^5}{T_A^{1.23}}[W/m - K]; T_A \geqslant 300[\mathrm{K}]$	Sim et al. [31]

In Eqs. (19) and (20), the subscript '*MC*' means raw data from MC simulation, which require proper normalizations given in Eqs. (23) and (24).

The MC simulation in this work also accounts for secondary electrons. These are energetic electrons generated within the medium due to momentum and energy transfer from primary electrons (i.e., electrons from the electron beam). Secondary electrons are capable of exiting the medium when their energies are sufficient to overcome the potential of the surface. Similarly, secondary electrons follow the same scattering probabilities as the primary electrons and contribute to the total deposition distributions. In the case when a secondary electron is generated, the electron density at that location will be reduced accordingly once the electron starts propagating elsewhere within the medium. When the secondary electron energy falls below the threshold value, Eq. (19) is applied at the corresponding location.

Secondary electrons can be generated from the inner-shell electrons or outer-shell electrons depending on the amount of energy transfer from the primary electrons. Here it is assumed that a secondary electron emerges from the inner-shell electrons when the amount of energy transfer, ΔE, is greater than the electron binding energy, E_b (i.e., ~100 eV in silicon); the energy of this secondary electron is given as $(\Delta E - E_b)$. If the energy transfer is smaller than E_b but larger than E_p, a secondary electron is generated with energy of $(\Delta E - E_p)$, where E_p is the peak plasmon energy. Electron energy is assumed to be lost if it is used to overcome the electron binding energy or to generate plasmon.

Upon hitting a surface, an electron ensemble is either reflected or refracted, which is determined by drawing a random number. This random number is compared against the transmission function [23], T:

$$T(E, \beta) = \begin{cases} \frac{4(1-U_0/E\cos^2\beta)^{1/2}}{[1+(1-U_0/E\cos^2\beta)^{1/2}]^2} & \text{if} \quad E\cos^2\beta > U_0, \\ 0 & \text{else.} \end{cases} \tag{21}$$

If the random number is smaller than T, then the ensemble is assumed refracted; otherwise, it is reflected. Once the ensemble is refracted, the exiting angle is altered to β' from its original angle β following the relation [3]:

$$\sqrt{E - U_0}\sin\beta' = \sqrt{E}\sin\beta. \tag{22}$$

It is clear from Eq. (21) that an electron ensemble would not exit the medium if its energy is below U_0, which is equivalent to the surface potential.

Once the tracings of the statistical ensembles are completed, the tallied electron density and energy are normalized using the total number of statistical ensembles considered, the total electron-beam energy, and the volume of the computational element in order to yield the statistical meaningful distributions. The normalizations are given as:

$$n_{MC,Nor}(x, y, z) = \frac{n_{MC,total}(x, y, z)}{NdV}, \tag{23}$$

$$E_{MC,Nor}(x, y, z) = \frac{E_{MC,total}(x, y, z)}{NE_{beam}dV}. \tag{24}$$

The distributions computed using Eqs. (23) and (24) are three-dimensional. Since the incident electron beam is perpendicular to the surface of the workpiece, it is possible to convert these distributions into two dimensions. However, we keep the generality of the simulations without the 2D conversion; this generality will enable us to consider an oblique electron beam in the future. In this study, since the EPHDEs are modeled in the *x*- and *z*-directions for the sake of simplicity and as our first approximation to produce insights to the electron-beam heating phenomena, the cross sections of these MC distributions at $y = 0$ are extracted and treated as the source generations in the EPHDEs (which are discussed in the next section); they are given as:

$$\dot{n}_{e,gen}(x, z) = \frac{I_{beam}}{e} n_{MC,Nor}(x, y = 0, z), \tag{25}$$

$$\dot{W}_{LO,gen}(x, z) = \frac{E_{beam}I_{beam}}{e} E_{MC,Nor}(x, y = 0, z), \tag{26}$$

where e is the coulomb charge, E_{beam} the initial beam energy, and I_{beam} the electric current of the beam. Eq. (25) is the generated local electron density while Eq. (26) gives the optical-phonon generation by the electron beam.

2.2. Electron–phonon hydrodynamic equations

When electrons lose energy until several electron-volts, electron–phonon interactions become important, and correct scattering cross sections are required to accurately represent the physics of scattering these electrons. Since electron–phonon scattering is greatly governed by the temperature inside the material, the temperature profiles need to be predicted accurately. This necessitates the use of quite general EPHDEs in order to correctly represent the physics of these electrons. Consequently, electron deposition distributions at low electron energy calculated by the MC simulation need to be transferred to the EPHDEs to further study the impact of the electron beam on the local temperature distribution.

Coupling between results from the MC simulation and the EPHDEs requires careful consideration in terms of electron density and energy. The MC simulation for the electron-beam propagation is constructed such a way that electrons with varying energy levels are considered where elastic and inelastic scatterings of electrons

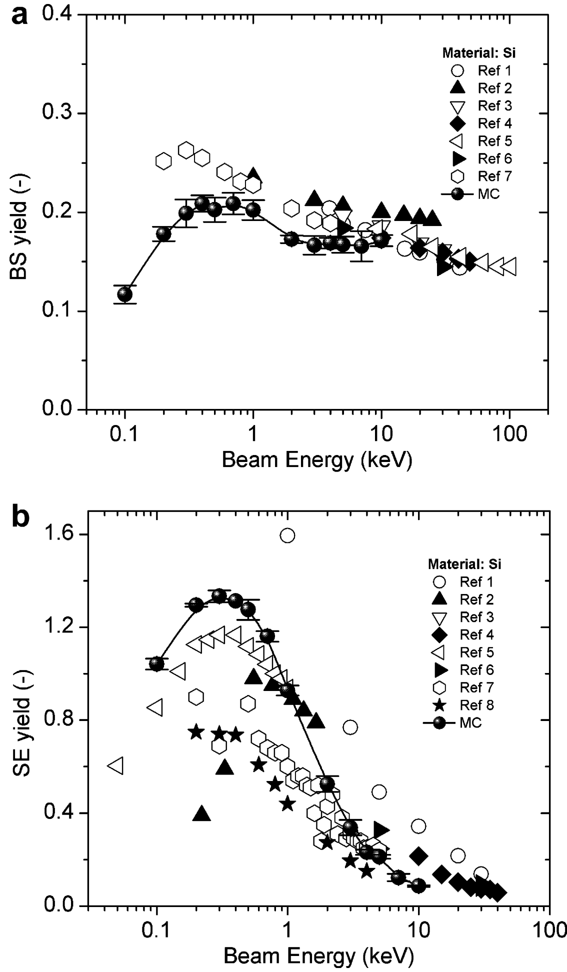

Fig. 4. (a) Backscattering yield comparison between this work and other results published in the literature. (b) Backscattering yield comparison between this work and other results published in the literature. Data points are directly obtained from the database compiled by Joy [17] (for the complete reference list, refer to the database). The backscattering yield includes electrons that are scattered back at the top surface with energy greater than 50 eV. Backscattered electrons with energy less than 50 eV contribute to the secondary electron yield.

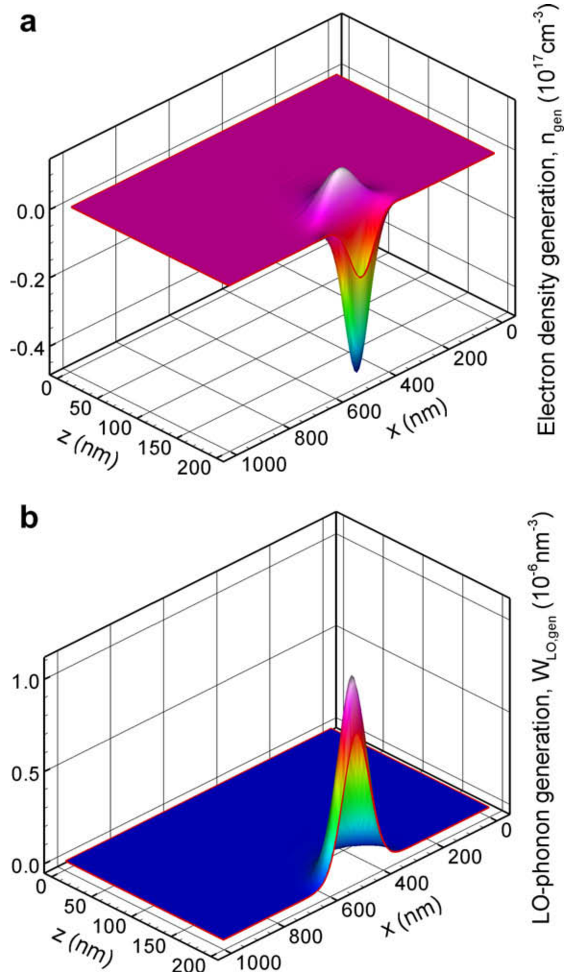

Fig. 5. The electron density deposition and the optical phonon generation distribution inside silicon (see Fig. 1 for inputs parameters).

are included. Essentially, MC simulation provides the solution for the EBTE, which is an intensity form of the Boltzmann transport equation (BTE) [5]. On the contrary, the EPHDEs are derived using the moments of the BTE where averaging effect over the energy spectrum of electrons is included [5], and they are quite useful for studying the interactions between electrons and phonons due to electric field and thermal gradient. In the EPHDEs, electrons and phonons are represented by the corresponding averaged density, momentum, and energy. As a result, detailed electron scattering directions and individual electron energy are not considered. Statistical results from the MC simulation of the electron beam are incorporated into the EPHDEs through source generation terms such as electron density and energy deposition distributions.

There are two important assumptions implied in this coupling approach. First of all, the directional and energy dependence of the electron propagation calculated in the electron-beam MC simulation become obsolete once the EPHDEs are utilized in which only average quantities are computed. Secondly, the induced electric potential and temperature should not have any influence on the high-energy electron trajectories in the MC simulation. This is true in this work especially the potential induced by the electron beam and the applied voltage are much less than the initial beam energy, as we shall see in the simulation results. Should this condition be violated, then a different coupling approach should be used. This condition will be not considered as it is out of scope in this study.

The general EPHDEs can be found in Refs. [5,11,19,24,25], and they can be simplified to yield:

$$\nabla^2\phi_e = \frac{e}{\varepsilon}(n_e - n_D);\ \vec{E} = -\nabla\phi, \tag{27}$$

$$\frac{\partial n_e}{\partial t} + \nabla_{\vec{r}}\cdot(\vec{v}_e n_e) = \dot{n}_{e,gen}, \tag{28}$$

$$\frac{\partial \vec{v}_e}{\partial t} = -\frac{e}{m_e}\vec{E} - \frac{k_B}{m_e n_e}\nabla_{\vec{E}}(n_e T_e) - \left(\frac{1}{\tau_m} + \frac{\dot{n}_{e,gen}}{n_e}\right)\vec{v}_e, \tag{29}$$

$$\frac{\partial T_e}{\partial t} + \nabla_{\vec{r}}\cdot(\vec{v}_e T_e) = \frac{1}{3}T_e\nabla_{\vec{r}}\cdot\vec{v}_e + \frac{2}{3n_e k_B}\nabla_{\vec{r}}\cdot(k_{T,e}\nabla_{\vec{r}}T_e) - \frac{T_e - T_{LO}}{\tau_{e-LO}} + \left(\frac{2}{\tau_m} - \frac{1}{\tau_{e-LO}} + \frac{\dot{n}_{e,gen}}{n_e}\right)\frac{m_e v_e^2}{3k_B} - \left(\frac{\dot{n}_{e,gen}}{n_e}\right)T_e, \tag{30}$$

$$\frac{\partial T_{LO}}{\partial t} = \frac{n_e m_e v_e^2}{2C_{LO}\tau_{e-LO}} - \frac{3n_e k_B(T_{LO} - T_e)}{2C_{LO}\tau_{e-LO}} - \frac{T_{LO} - T_A}{\tau_{LO-A}} + \frac{\dot{W}_{LO,gen}}{C_{LO}}, \tag{31}$$

$$\frac{\partial T_A}{\partial t} = \frac{1}{C_A}\nabla_{\vec{r}}\cdot(k_{T,A}\nabla_{\vec{r}}T_A) - \frac{C_{LO}(T_A - T_{LO})}{C_A\tau_{LO-A}}. \tag{32}$$

The momentum (P) and total energy (W) of the electrons are related to the velocity and density following these expressions:

$$\vec{P}_e = m_e n_e \vec{v}_e, \tag{33}$$

$$W_e = \frac{3}{2}n_e k_B T_e + \frac{1}{2}n_e m_e v_e^2. \tag{34}$$

Eq. (27) is the Poisson equation which determines the potential and the corresponding electric field inside the material based on the electron density distribution. Electron density is determined using the continuity equation, which is given by Eq. (28). The changes to the electron density due to the impinging electron beam are present in $\dot{n}_{e,gen}$ and it is obtained from the MC simulation (see Eq. (25)). Eq. (29) enforces momentum conservation of electrons and determines the electron velocity vector. Eqs. (30)–(32) are conservation of electron energy, optical phonon energy, and acoustic phonon energy. These equations are set up such a way that hot, energized electrons from the electron beam produce optical phonons inside the target object, which is described by $\dot{W}_{LO,gen}$ in Eq. (31) and determined from the MC simulation (see Eq. (26)). Eq. (30) captures the disturbance that the electron beam creates to the electron density and the electron temperature inside the material while these electrons exchange energy with optical phonons. Subsequently, through coupling between optical phonons and acoustic phonons, the acoustic phonon energy is increased. Detailed information regarding the derivation of these equations and how these averaged electron density, momentum, and temperatures are obtained are published in Ref. [5].

The coupling between optical phonons and acoustic phonons is done using a simple relaxation time approach. Since optical phonons have essentially zero velocity, the spatial diffusion term is omitted. Hot electrons typically emit optical phonons, which then increases the optical phonon temperature. Subsequently, optical phonons share the additional energy with acoustic phonons, which is accounted using the relaxation time $\tau_{LO\text{-}A}$. Unlike optical phonons, acoustic phonons possess finite thermal velocity. Therefore, the acoustic phonon thermal conductivity $k_{T,A}$ is used in the energy conservation equation of acoustic phonons to account for spatial heat diffusion. The relaxation time $\tau_{LO\text{-}A}$ is typically on the order of picoseconds and for silicon it is approximately 8 ps according to Majumdar [19]. There is no detailed information available regarding this issue; therefore, as our first approximation, we chose to use this value of 8 ps.

Several assumptions are implied in this version of the EPHDEs. First, the effective mass of the electrons is assumed to be a constant. Second, the advection term in the electron momentum conservation is neglected for the sake of simplicity. Third, heat conduction is treated as diffusive for both electrons and phonons. For electrons, such assumption is justified since wavelengths of electrons are generally much smaller than the thickness of the film considered in this work, and the heat transport is still diffusive [26]. However, for phonons, this assumption might be questionable because of the possibility of having ballistic/semi-ballistic nature of the transport as wavelengths of phonons are typically in the range of tens of nanometers to several microns depending on their

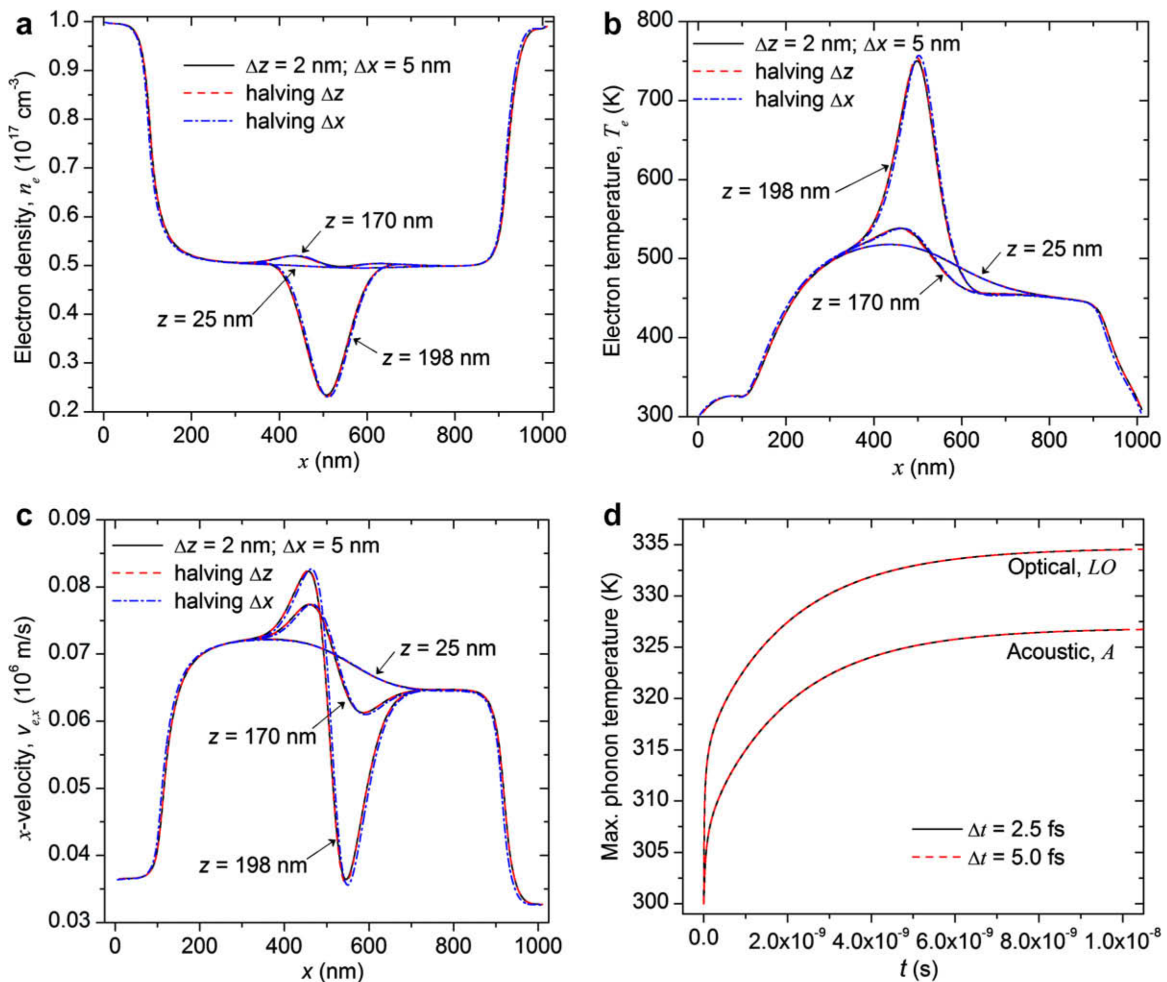

Fig. 6. (a) Electron density, (b) electron temperature, and (c) x-component of electron velocity at z = 25, 170, and 198 nm computed using different grid sizes. (d) The transient maximum phonon temperature computed using two different time steps is also given. The complete distributions of these plots along the x- and z-axis are given in the following figures.

energies, which may exceed the film thickness. Hence, ballistic/semi-ballistic behavior [11,25,27,28] could be important. In this work, this behavior is neglected as additional studies and careful considerations are required to correctly couple electrons and phonons when the transport is of ballistic nature, and these are left for future work.

Eqs. (28)–(32) require several thermophysical properties and they are listed in Table 1 following published data taken from various sources. The boundaries are of ohmic type, which assumes equilibrium at the contacts, and they can be expressed as follows:

$$\phi_e = \begin{cases} 0 & x = 0; \\ 1 & x = 1000\,\text{nm}. \end{cases} \tag{35}$$

$$n_D = \begin{cases} 3 \times 10^{17}\,\text{cm}^{-3} & 0 \leqslant x \leqslant 100\,\text{nm}; 900 \leqslant x \leqslant 1000\,\text{nm}; \\ 1.5 \times 10^{17}\,\text{cm}^{-3} & \text{else}. \end{cases} \tag{36}$$

$$T_e = 300\,\text{K} \quad \forall x = 0 \quad \text{and} \quad x = 1000\,\text{nm}, \tag{37}$$

$$T_{LO} = 300\,\text{K} \quad \forall x = 0 \quad \text{and} \quad x = 1000\,\text{nm}, \tag{38}$$

$$T_A = 300\,\text{K} \quad \forall x = 0 \quad \text{and} \quad x = 1000\,\text{nm}. \tag{39}$$

Insulated boundaries are assumed for the rest. Since potential, electron density, and electron temperature are held fixed at the boundaries, the velocities at the boundaries can be determined easily from the gradients of these values following Eq. (29).

In this work, we discretize the EPHDEs in x- and z-directions using a finite-difference method following the work published by various sources [29,32–38]. The time derivation is discretized using the first order approximation while the spatial discretization is performed using a second-order central-difference scheme. The upwind method is utilized to treat the flow field of electrons. The staggered grid scheme is used in the simulation [39]. In this scheme, scalar quantities are evaluated at the centers of the computational control volumes, and the velocity vectors and electric field are evaluated at the boundaries of the control volumes (i.e., between center points). The discretized equations are then solved using the successive over-relaxation scheme [40].

3. Results and discussions

3.1. Electron backscattering yields – verification of Monte Carlo simulation

The MC simulation code developed in this work was first verified against existing data obtained from the literatures. Fig. 4a shows the backscattering (BS) yield for silicon computed using the MC simulation developed in this work and published data obtained from the database compiled by Joy [17]. The BS yield is obtained by recording the total number of electrons backscattered off the medium with energy greater than 50 eV, and normalized by the total number of incident electrons. Five separate runs with 5000 statistical ensembles each are performed to access the statistical errors for the BS yield. Results from the MC simulation coincide with the

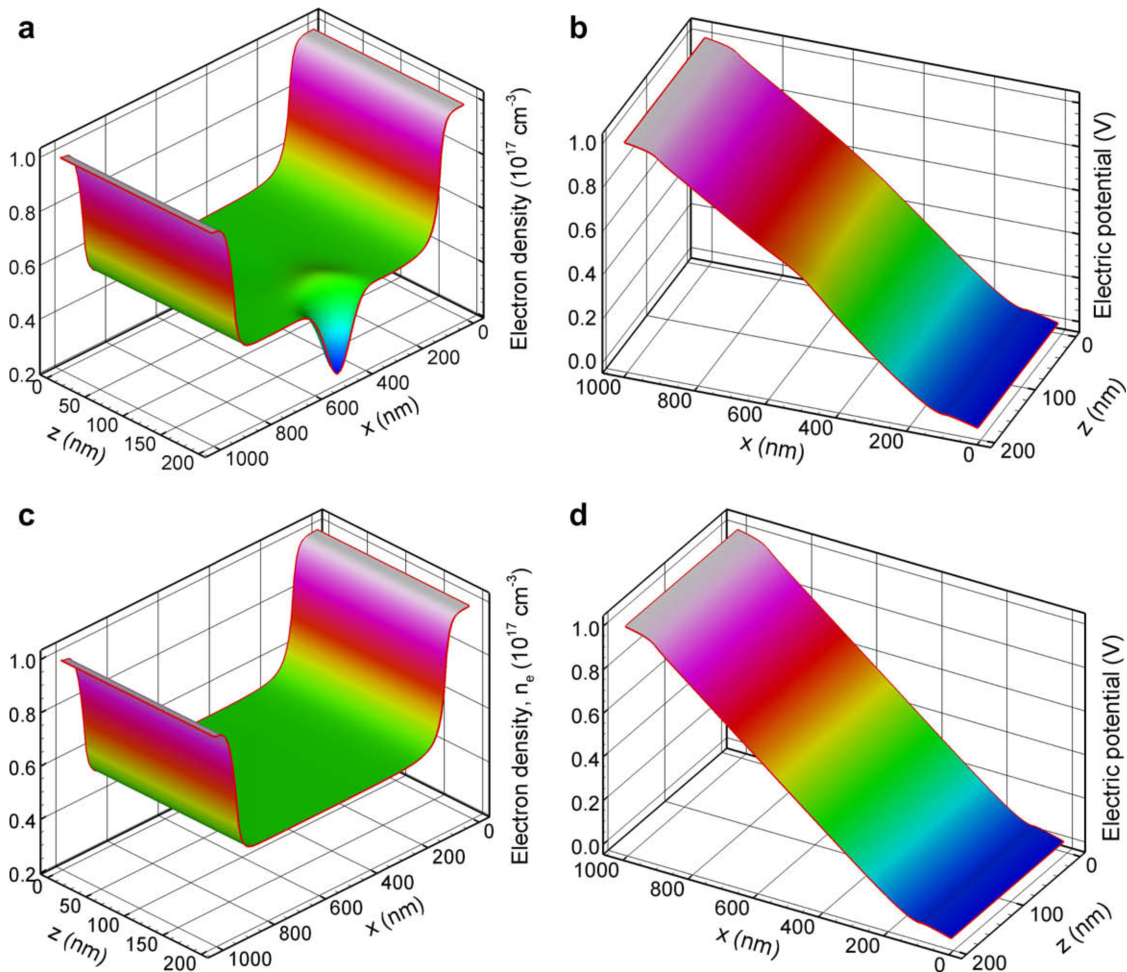

Fig. 7. The electron density and the electric potential inside the medium with (a and b) and without (c and d) the impinging electron beam (see Fig. 1 for inputs parameters).

various published data for electron-beam energies ranging from 0.1 to 10 keV. However, some discrepancies were found, particularly, in the energy range less than a few keV. In the current MC simulation, the code seems to produce more backscattered secondary electrons than primary electrons at low beam energy when compared to the published data. This reveals the weakness of the current MC simulation in predicting electron-beam propagation inside a semiconductor or an insulator for relatively low-energy electron beam.

A remedy for this is to account for the electron scatterings using different approach such as those described by Fitting's group [41–43], which uses quasi-elastic acoustic phonon scattering, optical phonons, and impact ionization instead of Mott scattering and dielectric energy losses. For backscattered electrons with energies less than 50 eV, which are called the secondary electron (SE) yield, a similar plot can be obtained (see Fig. 4b). In this case the SE yield for various electron-beam energies agree with the published data to an extent, verifying the correct implementation of the MC simulation. Even though there are some minor discrepancies between the published experimentally data and the MC simulation, the simulation in this work is sufficient to provide accurate estimates of the electron deposition distributions inside the thin film following the correct physics.

3.2. Monte Carlo simulation of electron deposition distributions

Electron deposition distributions for the case where impulse incident beam is considered are first obtained using 10,000 statistical ensembles. The initial electron-beam energy is set to 1 keV with a Gaussian beam radius of 100 nm and an electric current of 1 μA. These results are then convoluted using the Gaussian beam profile defined in Eq. (2) to produce the final desired distributions for the EPHDEs. The width of silicon thin film is assumed 1000 nm while the thickness is 200 nm. These dimensions ensure that transmission of the electron beam through the target is not possible at all. A voltage difference of 1 V is applied across the silicon thin film.

Fig. 5a depicts the normalized number of electron deposited inside the workpiece per unit volume inside the thin film. A positive electron deposition number indicates that there is accumulation of electrons while a negative electron deposition number implies that electrons are lost. It can be seen from the figure that electrons are depleted near the surface of incidence for the electron beam while electrons accumulate below the depletion region. Due to the initial high-energy electrons, secondary electrons are generated near the surface, and these electrons are capable of propagating deeper into the medium or leaving the surface depending on their energies; hence, depletion occurs. On the other hand, primary/secondary electrons penetrate into the material and reside there after suffering series attenuations, which then create the region of charge accumulation as evident in the figure. The corresponding optical phonon generation distribution inside silicon is shown in Fig. 5b. As expected, the optical phonon generation distribution inside the workpiece concentrates near the area of incidence following a Gaussian-like profile. The distribution peaks near the surface and decreases rapidly as the distance increases.

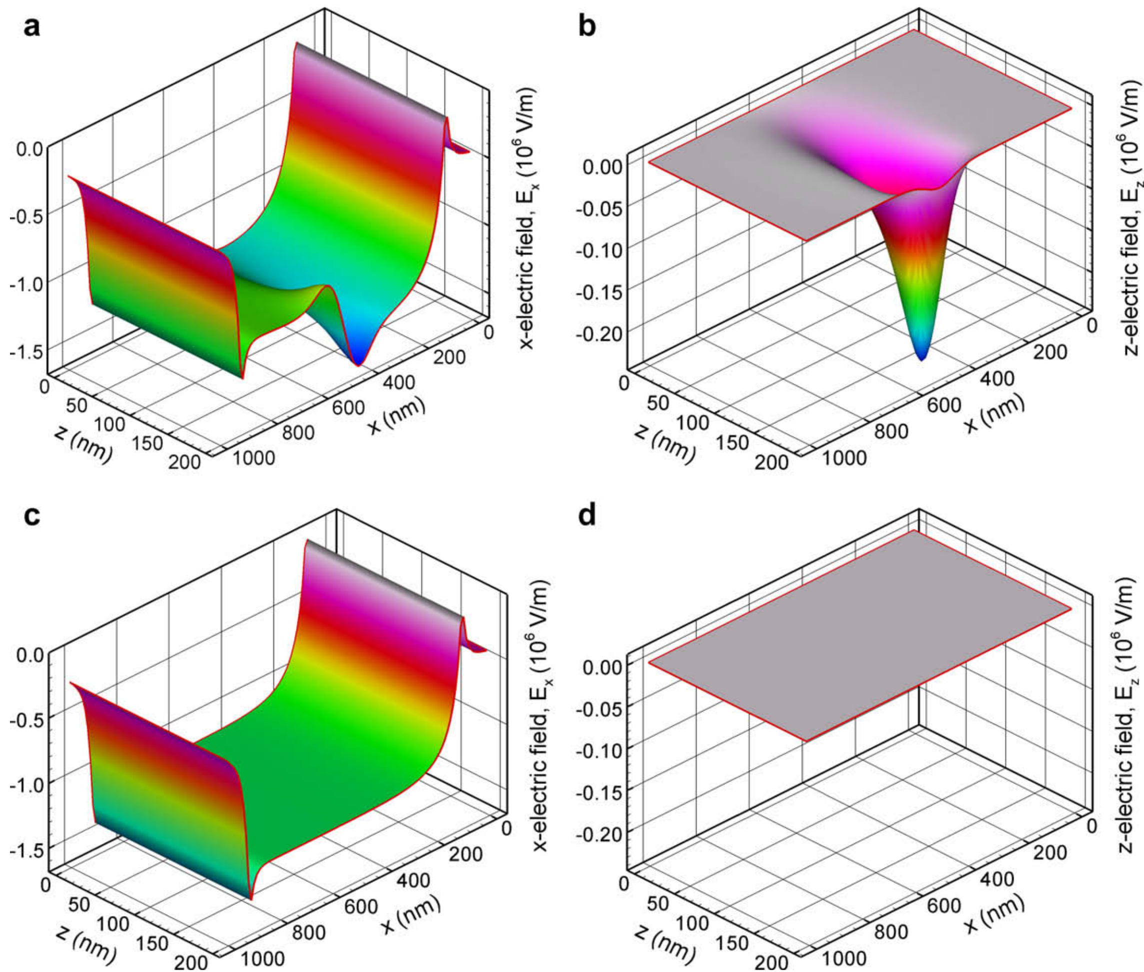

Fig. 8. The electric field distribution inside silicon with (a and b) and without (c and d) the incident electron beam (see Fig. 1 for inputs parameters).

The two computational parameters that greatly influence the electron density and the optical phonon generation distributions are the initial energy of the electron beam and the incident beam profile. When the initial electron-beam energy is higher, the distributions would be stretched in the direction of penetration since the depth of penetration is increased. In addition, these distributions can be stretched in the lateral direction as well by manipulating the Gaussian-beam radius. Larger radius of the beam creates wider spread of the incident electrons as well as the optical phonon generation.

3.3. Electrical and thermal responses of silicon

By coupling the results obtained from the MC simulation, electron and phonon temperatures inside silicon can be determined by taking the electrical response of the workpiece into consideration and using the EPHDEs. After conducting several numerical experiments, the grid resolutions are determined to be $\Delta x = 5$ nm and $\Delta z = 2$ nm. The time step used in the simulation is set to be $\Delta t = 2.5$ fs. Further reduction in the grid step sizes and time step does not improve the accuracy of the simulation results significantly. Fig. 6 shows comparisons between results obtained using different grid step sizes at various z-locations (i.e., $z = 25$, 170, and 198 nm). By halving the grid step size in the x-direction while maintaining other parameters constant, it is observed that the electron density, electron temperature, and x-component of electron velocity profiles at different z-locations remain almost identical, indicating the convergence of the solution. Similarly, halving the grid step size in the z-direction yields the identical distributions as evident in the figure. In addition, the transient maximum phonon temperature converges to the same profile when the time step is halved from 5 fs to 2.5 fs. Other simulation plots are not given here to keep the manuscript within reasonable.

Fig. 7 depicts the electron density and the voltage distributions as a result of electron-beam penetration. For the sake of comparison, simulation results of the case without the incident electron beam are shown in the corresponding figure to indicate the degree of perturbation to the computed distributions when an electron beam is present. As observed from Fig. 5, electrons are depleted around the area of incident beam; this is expected as it correlates directly with electron density deposition plotted in Fig. 5. The depletion is noticeable at the vicinity of $x = 500$ nm; however, the change in the local electron density does not significantly change the local voltage distribution. There is only a slight alteration of the voltage curve near $x = 500$ nm, yet, the change is minor and almost unnoticeable for the case we consider here.

The electric field distributions inside the workpiece are depicted in Fig. 8. The field is decomposed into x- and z-components. In the case where the electron beam is not present, the x-electric field distribution remains smooth near the center of the top surface. When an electron beam impinges on the surface, the electric field distributions are altered. These perturbations are induced such a way that electrons are being pushed away from the area of incidence of the beam. In addition, the presence of the electron beam induces an electric field distribution in the z-direction. It is clear that electrons are being driven away by the energetic electron

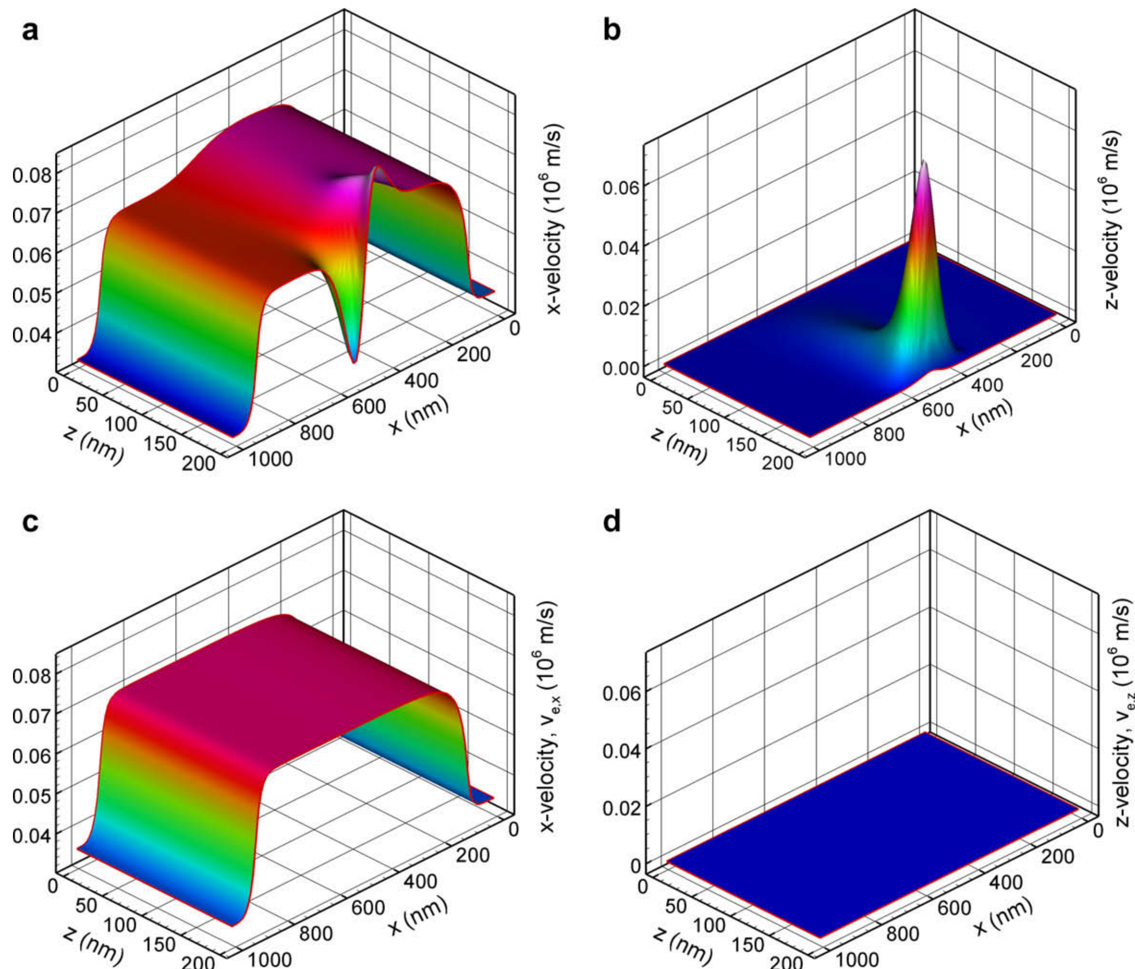

Fig. 9. The velocity profiles of electrons due to applied voltage with (a and b) and without (c and d) impinging electron beam (see Fig. 1 for inputs parameters).

beam, and hence the depletion region is created as shown in Fig. 7. The corresponding velocity distributions are depicted in Fig. 9. In Fig. 9c, we see that electrons accelerate starting from $x = 0$ boundary and reach to a uniform velocity of approximately 0.07×10^6 m/s, then followed by a deceleration near $x = 1000$ nm boundary when there is no external perturbation for an electron beam. With an impinging electron beam near the middle of the workpiece (i.e., $x \sim 500$ nm, $y = 200$ nm in Fig. 9a and b), the local velocity field is altered where electrons are being depleted near the depth of penetration of the beam due to the generated secondary electron that escape the surface.

Fig. 10 depicts the temperature distributions of electrons, optical phonons, and acoustic phonons with and without the impinging electron beam. We observe that by applying a potential difference of 1 V, the electron temperature reaches around 500 K while the optical and acoustic phonon temperatures do not break 1 K beyond room temperature at steady-state condition. However, when an electron beam with an initial energy of 1 keV impinges on

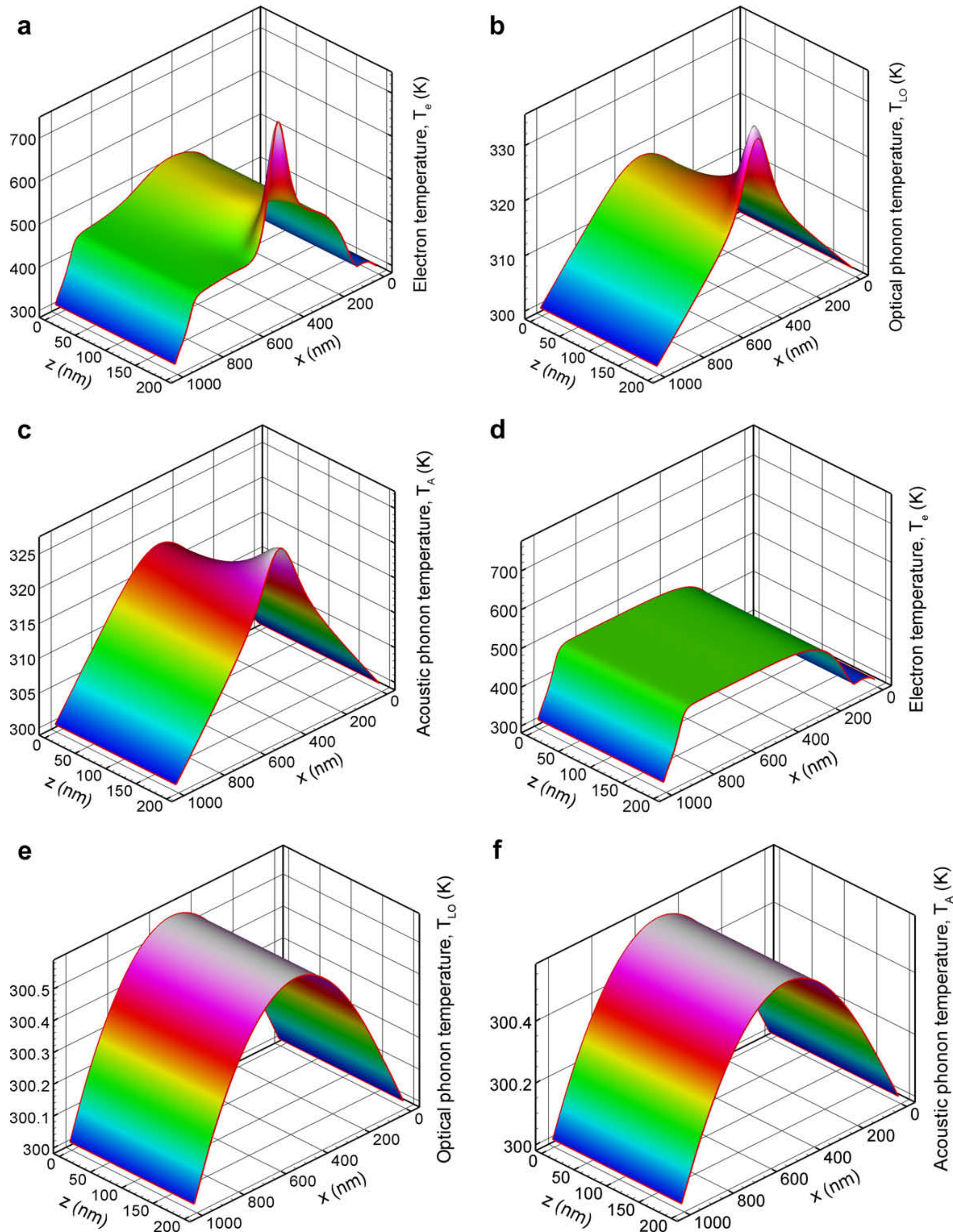

Fig. 10. The electron, optical and acoustic phonon temperatures inside the medium with (a–c) and without (d–f) impinging electron beam (see Fig. 1 for inputs parameters).

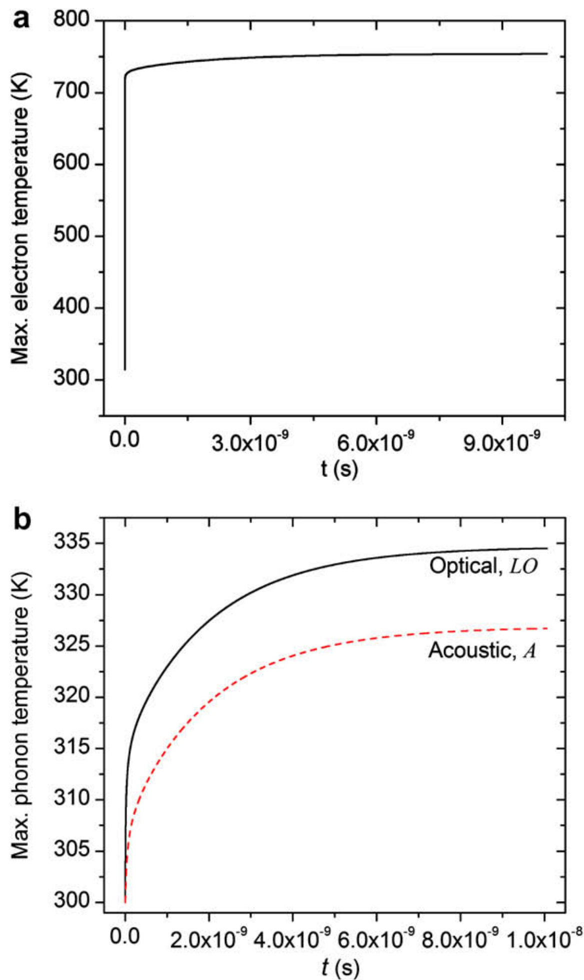

Fig. 11. The transient maximum electron and phonon temperatures within silicon for electron-beam and Joule heating (see Fig. 1 for inputs parameters).

the workpiece, the local electron temperature at the location where the beam strikes is raised to approximately 750 K. This is accompanied by about 35 K increase in the local optical-phonon temperature and 25 K in the local acoustic phonon temperature. It is obvious that the optical-phonon temperature is increased as a result of the LO-phonon generation by the electron beam, and this additional energy is then transferred to the acoustic mode through phonon-phonon collisions. However, the local temperature increase in electrons is caused indirectly by the electron beam. From the MC results given in Fig. 5, we observe that the material is losing electrons due to the secondary electron emission layers below the surface. The local electron density decreases while the applied potential difference remains unaltered. As a result, the local electron temperature around the depletion region increases.

The transient maximum electron and phonon temperatures within silicon workpiece as a result of electron-beam heating are given in Fig. 11. Notice that the electron temperature reaches steady-state value a few nanoseconds faster than the phonon temperatures, and these transient predictions are mostly sensitive to the input parameters. As discussed before, the applied voltage and the current of the electron beam are increased gradually in order to avoid the abrupt initial conditions which might cause convergence problem in the EPHDEs. Given the set of input parameters used in this work, the optical-phonon temperature is higher than the acoustic-phonon temperature at all times because of the continuous electron-beam heating.

4. Conclusions

We have discussed a detailed analysis of the electrical and thermal responses of a silicon workpiece to an impinging electron beam and Joule heating. The model is based on the numerical solution of EPHDEs and MC simulation of EBTE. A MC model was developed for this purpose, which accounts for the secondary electron generation and utilizes Mott's scattering cross-section and the Penn's dielectric function. Energetic electrons originated from the electron beam were traced statistically using the scattering probabilities derived from the Mott's cross section, the energy-loss function and the electron-optical phonon interaction. Secondary electrons were treated following similar scattering probabilities of the primary electrons. The backscattering and secondary electron yields were verified against the existing data published in the literature. A number of steps were introduced to calculate the electron density and optical-phonon generation within silicon, which served as the sources of heat generation in the EPHDEs. The coupling between the statistical results from the MC simulation and the EPHDEs was done carried on assuming that neither the thermal gradient nor the electric field induced by the electron beam were large enough to alter the propagation of the beam. Hence, the electron density and the optical phonon generation distributions remained unaltered throughout the hydrodynamic simulations.

Results show that an electron beam is capable of creating a depletion region near the surface of incidence while causing non-equilibrium between electron and phonon temperatures. The initial beam energy used for these results is 1 keV with a current of 1 μA and a Gaussian radius of 100 nm. When it is applied to a silicon target of 1000 × 200 nm dimensions, maximum local electron temperature is raised to 750 K and that of optical-phonon temperature to 335 K. An increase of 25 K in the local acoustic temperature is also observed. These results suggest a potential application where an electron beam can be used to locally alter the electron density profile while the device is operating at a given applied voltage. Results for other electron beam energies and materials are not included in this paper. Additional simulations with different materials and design parameters in terms of the electron beam and dimensions of the structure will be reported in another work in the future.

The solution methodology can be further improved by iteratively calculating the deposition distributions while solving the EPHDEs, although such an approach is usually computational intensive. In addition, the deposition distributions obtained from the MC simulation can be further improved by using a different approach to treat the elastic and inelastic scattering (i.e., quasi-phonon scattering model) as suggested by Fitting's group [41–43]. The physics of the EPHDEs can also be enhanced by replacing the phonon conservation equations with a MC simulation in phonon transport [28] to account for the ballistic/semi-ballistic behavior of phonons.

Acknowledgments

This research work was supported in part by a grant from the Kentucky Science and Engineering Foundation as per Grant Agreement KSEF-1147-RDE-009 with the Kentucky Science and Technology Corporation.

References

[1] N. Taniguchi, M. Ikeda, I. Miyamoto, T. Miyazaki, Energy-Beam Processing of Materials: Advanced Manufacturing Using Various Energy Sources, Oxford University Press, New York, 1989.
[2] R.F. Egerton, Electron Energy Loss Spectrometry in the Electron Microscope, Second ed., Plenum Press, New York, 1996.

[3] Z.J. Ding, R. Shimizu, A Monte Carlo modeling of electron interaction with solids including cascade secondary electron production, Scanning 18 (1996) 92–113.
[4] D.C. Joy, Monte Carlo modeling for electron microscopy and microanalysis, Oxford University Press, New York, 1995.
[5] B.T. Wong, M.P. Mengüç, Nanoscale Thermal Transport for Applications in Micro/Nanomachining, Springer, 2008.
[6] B.T. Wong, M.P. Mengüç, R.R. Vallance, Nano-scale machining via electron beam and laser processing, ASME J. Heat Transfer 126 (4) (2004) 566–576.
[7] B.T. Wong, M.P. Mengüç, R.R. Vallance, Sequential nano-patterning using electron and laser beams: a numerical methodology, J. Comput. Theor. Nano-Sci. 3 (2) (2006) 1–12.
[8] B.T. Wong, M.P. Mengüç, R.R. Vallance, Nanoscale thermal transport induced by electron-beam, Int. J. Heat Mass Transfer 50 (2007) 5099–5107.
[9] B.T. Wong, M.P. Mengüç, Comparison of Monte Carlo techniques to predict the propagation of a collimated beam in participating media, Numer. Heat Transfer B 42 (2002) 119–140.
[10] B.T. Wong, M.P. Mengüç, Monte Carlo methods in radiative transfer and electron-beam processing, J. Quant. Spectrosc. Radiat. Transfer 84 (2004) 437–450.
[11] G. Chen, Nanoscale Energy Transport and Conversion, Oxford Press, New York, 2005.
[12] N.F. Mott, H.S.W. Massey, The Theory of Atomic Collisions, Clarendon Press, Oxford, 1965.
[13] D.R. Penn, Electron mean free path calculations using a model dielectric function, Phys. Rev. B 35 (1987) 482–486.
[14] D. Pines, P. Nozières, The Theory of Quantum Liquids, Benjamin, New York, 1966.
[15] L. Wang, S.L. Jacques, L. Zheng, MCML-Monte Carlo modeling of light transport in multi-layered tissues, Comput. Method Programs Biomed. 47 (1995) 131–146.
[16] S.R. Lin, N. Sherman, J.K. Percus, Nucl. Phys. 45 (1963) 492.
[17] D.C. Joy, Electron solid interaction databse (2001). Available from: <http://web.utk.edu/srcutk/htm/interact.htm>.
[18] E.D. Palik, Handbook of Optical Constants of Solids, Academic Press, New York, 1985.
[19] A. Majumdar, in: C.L. Tien (Ed.), Microscale Energy Transport, Begell House, New York, 1998. pp. 1-93.
[20] P.H. Nguyen, K.R. Hofmann, G. Paasch, Comparative full-band Monte Carlo study of Si and Ge with screened pseudopotential-based phonon scattering rates, J. Appl. Phys. 94 (1) (2003) 375–386.
[21] P.H. Nguyen, K.R. Hofmann, G. Paasch, Full-band Monte Carlo model with screened pseudopotential based phonon scattering rates for a lattice with basis, J. Appl. Phys. 92 (9) (2002) 5359–5370.
[22] M.V. Fischetti, S.E. Laux, Monte Carlo analysis of electron transport in small semiconductor devices including band-structure and space-charge effects, Phys. Rev. B 38 (14) (1988) 9721–9745.
[23] C. Cohen-Tannoudji, B. Diu, F. Laloe, Quantum Mechanics, Hermann, Paris, 1977.
[24] K. Blotekjaer, Transport equations for electrons in two-valley semiconductors, IEEE Trans. Electron Devices ED-17 (1) (1970) 38–47.
[25] Z.M. Zhang, Nano/Microscale Heat Transfer, McGraw-Hill, New York, 2007.
[26] B.T. Wong, M.P. Mengüç, Electronic thermal conduction in thin gold films, in: ASME Summer Heat Transfer Conference, Las Vegas, Nevada, 2003.
[27] D. Lacroix, K. Joulain, D. Lemonnier, Monte Carlo transient phonon transport in silicon and germanium at nanoscales, Phys. Rev. B 72 (2005) 064305.
[28] S. Mazumder, A. Majumdar, Monte Carlo study of phonon transport in solid thin films including dispersion and polarization, J. Heat Transfer 123 (2001) 749–759.
[29] V. Romano, G. Russo, Numerical solution for hydrodynamical models of semiconductors, Math. Models Methods Appl. Sci. 10 (7) (2000) 1099–1120.
[30] J.M. Ziman, Electrons and Phonons, Oxford University Press, London, 1960.
[31] H.S. Sim, S.H. Lee, K.G. Kang, Femtosecond pulse laser interactions with thin silicon films and crater formation considering optical phonons and wave interference, Microsyst. Technol. 14 (2008) 1439–1446.
[32] A. Aste, R. Vahldieck, Time-domain simulation of the full hydrodynamic model, Int. J. Numer. Model. Electron. Netw Devices Fields 16 (2003) 161–174.
[33] A. Aste, R. Vahldieck, M. Rohner, Full Hydrodynamic Simulation of GaAs MESFET's, Int. J. Numer. Model. Electron. Netw. Devices Fields 17 (2004) 43–59.
[34] K. Fushinobu, A. Majumdar, K. Hijikata, Heat generation and transport in submicron semiconductor devices, J. Heat Transfer 117 (1995) 25–31.
[35] A. Majumdar, K. Fushinobu, K. Hijikata, Effect of gate voltage on hot-electron and hot-phonon interaction and transport in a submicrometer transistor, J. Appl. Phys. 77 (12) (1995) 6686–6694.
[36] C.M. Snowden, Semiconductor Device Modelling, Peter Peregrinus Ltd., London, 1988.
[37] K. Tomizawa, Numerical Simulation of Submicron Semiconductor Devices, Artech House, Inc., Norwood, 1993.
[38] S. Yoganathan, S.K. Banerjee, A new decoupled algorithm for nonstationary, transient simulations of GaAs MESFET's, IEEE Trans. Electron Devices 39 (7) (1992) 1578–1587.
[39] S.V. Patankar, Numerical Heat Transfer and Fluid Flow, McGraw-Hill Book Company, New York, 1980.
[40] J.H. Matthews, K.D. Fink, Numerical Methods Using Matlab, third ed., Prentice Hall, Inc., New Jersey, 1999.
[41] H.J. Fitting, E. Schreiber, I.A. Glavatskikh, Monte Carlo modeling of electron scattering in nonconductive specimens, Microsc. Microanal. 10 (2004) 764–770.
[42] H.J. Fitting, E. Schreiber, J.-C. kuhr, A. Von Czarnowski, Attenuation and escape depths of low-energy electron emission, J. Electron Spectrosc. Relat. Phenomena 119 (2001) 35–47.
[43] E. Schreiber, H.J. Fitting, Monte Carlo simulation of secondary electron emission from the insulator SiO_2, J. Electron Spectrosc. Relat. Phenomena 124 (2002) 25–37.